IOP Publishing

Hypersonic Meteoroid Entry Physics

Gianpiero Colonna, Mario Capitelli and Annarita Laricchiuta

Chapter 3

Properties of meteoroids from forward scatter radio observations

Hervé Lamy

3.1 Radio meteor theory

When a meteoroid enters the Earth's atmosphere with velocities in excess of ~10 km s^{-1}, it impacts the atoms and molecules of the upper atmosphere with a kinetic energy large enough to ionize them. It also heats up to high temperatures and starts to ablate. As a result, a trail of ions and electrons forms along the trajectory path behind the meteoroid.

If a radio wave of a given frequency is sent towards space from a ground-based transmitter, it can be temporarily reflected by the meteor trail towards the ground. The incident radio wave is scattered only by electrons as ions are too heavy. Under some geometrical conditions (see below), it can be recorded by a receiver tuned to the same frequency. The signal recorded at the receiving station is called a meteor trail echo. Its duration is directly related to the lifetime of the meteor trail as the electrons tend to quickly scatter into the neutral ambient atmosphere. A meteor radar corresponds to the case where the transmitter and the receiver are located at the same place. When the transmitter and receiver(s) are not on the same site, we talk about forward scatter observations (see figure 3.1) which is the topic of this chapter.

Meteor echoes are usually classified into two categories called underdense and overdense, according to the value of the line electron density α (expressed in number of electrons per meter). This is based on McKinley's [1] classical radio meteor theory, where it is first assumed that the trail is a stationary straight line of electrons, a hypothesis made because the longitudinal extent of the trail (typically a few kilometers to a few tens of kilometers) is much larger than its radial extent (from a few tens of centimeters to a few meters). Additional factors are then included, such as the initial radius effect, to take into account the finite radial extent of the trail (assumed to be cylindrical), and the ambipolar diffusion to model the scattering of trail electrons into the ambient neutral atmosphere. The typical duration of

doi:10.1088/2053-2563/aae894ch3

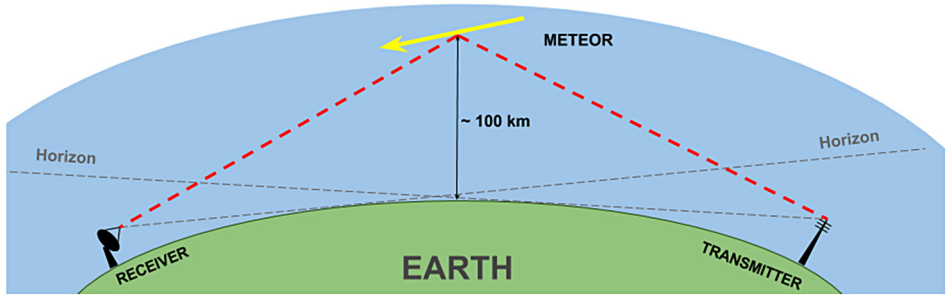

Figure 3.1. Sketch of the general principle of radio forward scatter observations.

underdense meteor echoes is a fraction of a second while overdense meteor echoes can typically last from ~one second to a few tens of seconds.

Underdense meteor echoes have typical line electron densities $\alpha < 10^{13}\,\mathrm{e} - \mathrm{m}^{-1}$ while overdense meteor echoes have $\alpha > 10^{15}\,\mathrm{e} - \mathrm{m}^{-1}$. There are of course a lot of meteor echoes with intermediate electron line densities for which the physics is more complex. Some recent developments (e.g. [2]) are trying to model these meteor echoes, but this is beyond the goal of this chapter. From a physics point of view, the radio wave can penetrate underdense meteor trails and is scattered by individual electrons while for overdense meteor trails, the electron density is large enough that the dielectric constant of the medium becomes negative and the trail behaves as a plasma. The classical theory of McKinley [1] models the overdense meteor echoes as if the radio wave was reflected on the surface of an expanding metallic cylinder. As we will see below, this theory for overdense meteor echoes has limited applications as it is too simplistic and does not include additional phenomena.

One fundamental property of underdense meteor echoes is that the reflection of the radio wave is specular, which means that the majority of the received power reflected off the trail occurs when the so-called specular reflection point is created on the meteoroid path. The position of this reflection point is easy to determine as it is the point along the meteoroid path that is tangential to an ellipsoid whose foci are the transmitter and the receiver (see figure 3.2).

This property simply results from adding elemental small contributions from each electron individually along the path. The vast majority of the power actually comes from a small region centered on the specular reflection point and called the first Fresnel zone, whose size depends mostly on the meteor speed and on the wavelength of the radio wave. Contributions from other parts of the meteor trail can add constructively or destructively to this main signal, leading to so-called Fresnel oscillations in the signal.

An important consequence of the specular reflection is that a given system made of a transmitter and one receiver cannot detect all meteors. This is illustrated in figure 3.3. If the reflection point is located too high in the atmosphere (bottom case), the atmosphere is too thin at these altitudes such that the created ionization is not large enough to reflect a detectable amount of power. On the other hand, if the reflection point is located too low in the atmosphere (top case), the meteoroid might be completely ablated before this point is created and therefore no signal at all will be detected at the receiver. In figure 3.3, what is called the 'meteor zone' refers to a

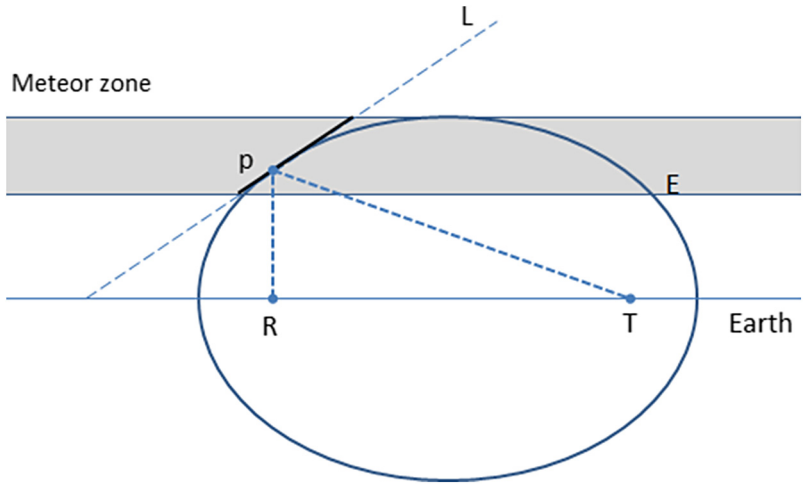

Figure 3.2. Illustration of the specularity condition. The specular reflection point p is the point along the meteoroid path L that is tangential to the ellipsoid E whose foci are the transmitter T and receiver R.

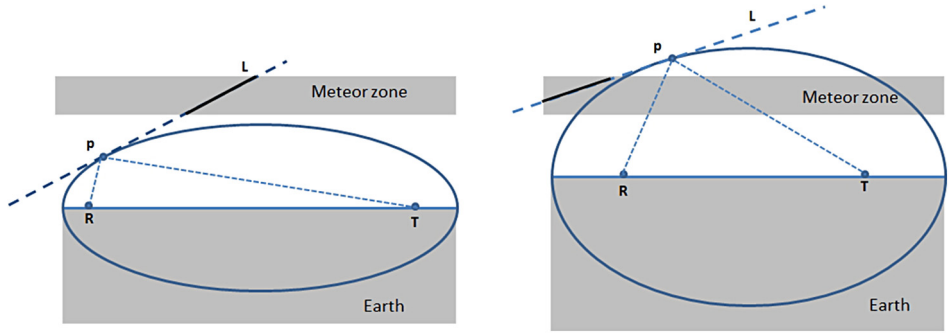

Figure 3.3. Consequences of the specularity condition. For given L, T and R, if the specular point p is too low (left) or too high (right), no signal will be recorded at T.

region in altitude where most meteor echoes should occur and can roughly be considered as 85–110 km.

The theory of forward scatter of radio waves has been developed by McKinley [1] as an extension of the classical theory for back scatter/radar systems. It provides formulas for the power profile, namely the amount of power in the meteor echo as a function of time.

For underdense meteor echoes, the power at the receiver is given by

$$P_R = \frac{P_T G_T G_R \lambda^3 r_e^2 \alpha^2 \sin^2(\gamma)}{16\pi^2 R_T R_R (R_T + R_R)(1 - \sin^2(\phi)\cos^2(\beta))} \exp\left[-\frac{8\pi^2 r_0^2}{\lambda^2 \sec\phi}\right] \exp\left[-\frac{32\pi^2 D_a t}{\lambda^2 \sec\phi}\right] \{C^2 + S^2\}, \tag{3.1}$$

where P_T is the power sent by the transmitter, G_T and G_R are the antenna gains for the transmitter and receiver in the directions to the reflection point, λ is the wavelength, r_e is the classical radius of the electron, α is the electron line density, γ is the polarization of the radio wave, R_T and R_R are the distances between, respectively, the transmitter/receiver and the specular reflection point, ϕ is half of the scattering angle of the radio wave and β is the inclination of the meteor trail with respect to the propagation plane of the radio wave. The geometrical parameters are illustrated in figure 3.4.

The first term in equation (3.1) is the peak value obtained when the specular reflection point is created and assuming all electrons lie on a straight line. The actual peak value is corrected by the initial radius r_0 that takes into account that trail electrons are not located on a single line but inside a cylinder, which reduces the strength of the signal and leads to the first exponential in equation (3.1). The second exponential depends on time t and is due to the diffusion of trail electrons in the neutral atmosphere. D_a is the ambipolar diffusion coefficient. The final terms in equation (3.1), C and S, are Fresnel integrals:

$$C = \int \cos\frac{\pi x^2}{2}dx \quad S = \sin\frac{\pi x^2}{2}dx, \tag{3.2}$$

where $x = 2s/\sqrt{R_F\lambda}$ is the Fresnel length, s is the distance along the trail measured from the specular reflection point, counted positively in the direction where the meteoroid is moving, and R_F is the size of the first Fresnel zone. This term is at the origin of the Fresnel oscillations which superimposes on the main signal. Indeed, every time a new Fresnel zone is created along the meteoroid path, it creates signals

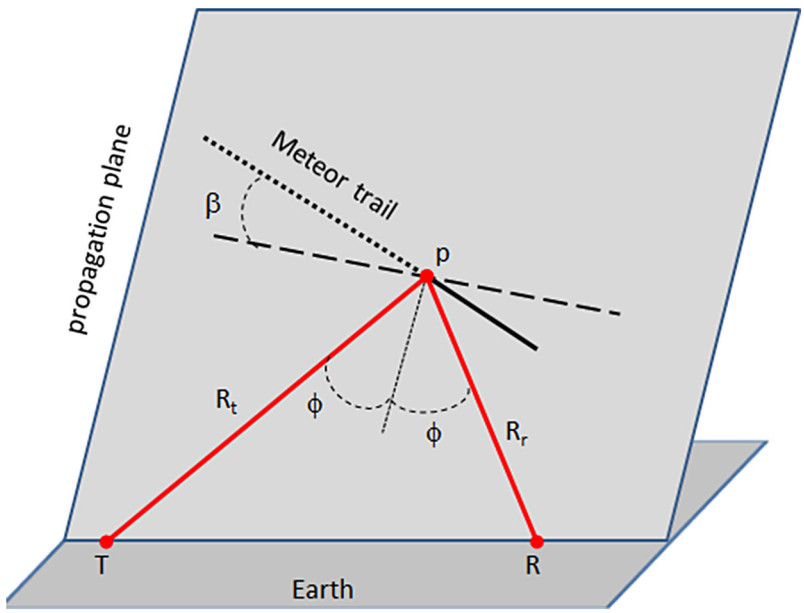

Figure 3.4. Geometrical parameters for forward scattering of radio waves.

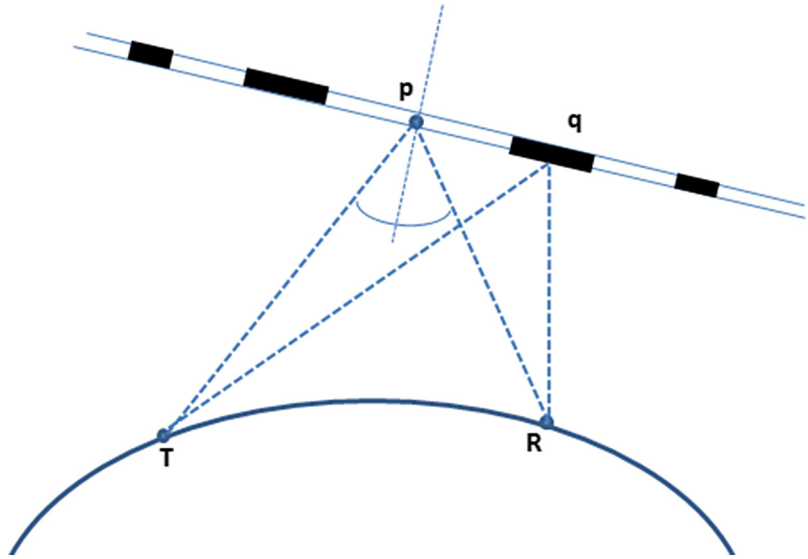

Figure 3.5. Illustration of Fresnel zones. The main Fresnel zone is centered on the specular reflection point *p*. Fresnel zones with constructive interference with the main signal are in white while those leading to destructive interference are in black.

which are alternatively in phase and out of phase with the main signal and leads to an increase/decrease of the total power. An example is given in figure 3.5 where the contribution from point *q* adds up to the main signal coming from point *p* in a destructive way, leading to a slight decrease of the power. Along a given meteoroid path and knowing the speed of the object, the positions of the Fresnel zones can be determined. In figure 3.5, the Fresnel zones leading to constructive interference with the main signal are depicted in white and those leading to destructive interference in black.

An example of an underdense meteor echo is shown in figure 3.6.

For overdense meteor echoes, the power at the receiver is given by

$$P_R = \frac{P_T G_T G_R \lambda^2 \cos\phi \sin^2\gamma}{32\pi^2 R_T R_R (R_T + R_R)(1 - \sin^2\phi \cos^2\beta)} r_c, \tag{3.3}$$

where r_c is the critical radius of the 'metallic' cylinder where the dielectric constant becomes negative,

$$r_c = \sqrt{r^2 \ln \frac{\alpha r_e \lambda^2 \sec^2\phi}{\pi^2 r^2}}, \tag{3.4}$$

where r is the radial distance perpendicular to the path. This model is rather poor as it neglects a number of phenomena, e.g. it does not take into account the effect of external parts of the cylinder which become increasingly underdense with time. More important, it neglects the influence of high-altitude mesospheric/thermospheric shear winds which can reach speeds from tens to a few hundreds of meters

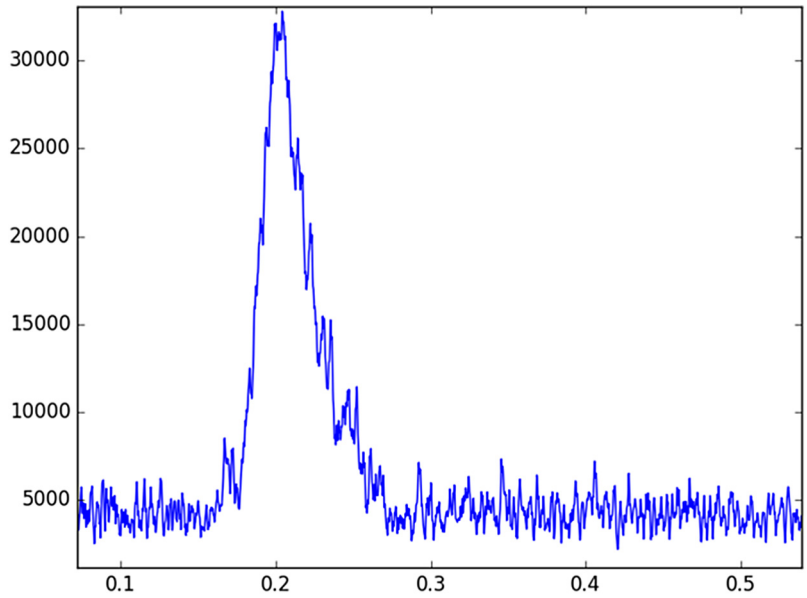

Figure 3.6. Typical underdense meteor echo. The vertical axis is power in arbitrary units while the horizontal axis is time in seconds.

per second. They can break the cylindrical trail into multiple parts and hence create multiple specular reflection points. The multiple reflections can then interfere constructively or destructively and lead to a much more complex power profile than the one modeled by equations (3.3) and (3.4).

An example of an overdense meteor echo is shown in figure 3.7.

Meteor trail echoes form the vast majority of meteor echoes detected by meteor radars such as, e.g., the Canadian Meteor Orbit Radar (CMOR, e.g. [3]) or by the Belgian Radio Meteor Stations (BRAMS) network that will be described in detail in the next section. Another type of meteor echo, mostly observed with larger objects, is the head echo which occurs when the incoming radio wave is reflected upon the ionized region forming in front of the meteoroid. This region moves at the same high speed ($>\sim 10\ \mathrm{km\ s^{-1}}$) as the meteoroid itself while the speed of the meteor trail depends mostly on the speed of high-altitude mesospheric/thermospheric winds. Consequently, the Doppler effects associated with these two types of meteor echoes are very different and allow one to easily discriminate them. Head echoes will not be discussed in detail in this chapter. Only a few examples of observations will be given in the section about optical versus radio observations of meteors.

3.2 The BRAMS project

3.2.1 The BRAMS network

BRAMS is a Belgian radio network using forward scatter techniques to detect and study meteoroids. It uses a dedicated transmitter located at the Geophysical Center in Dourbes in the south of Belgium and 26 identical receiving stations spread all over

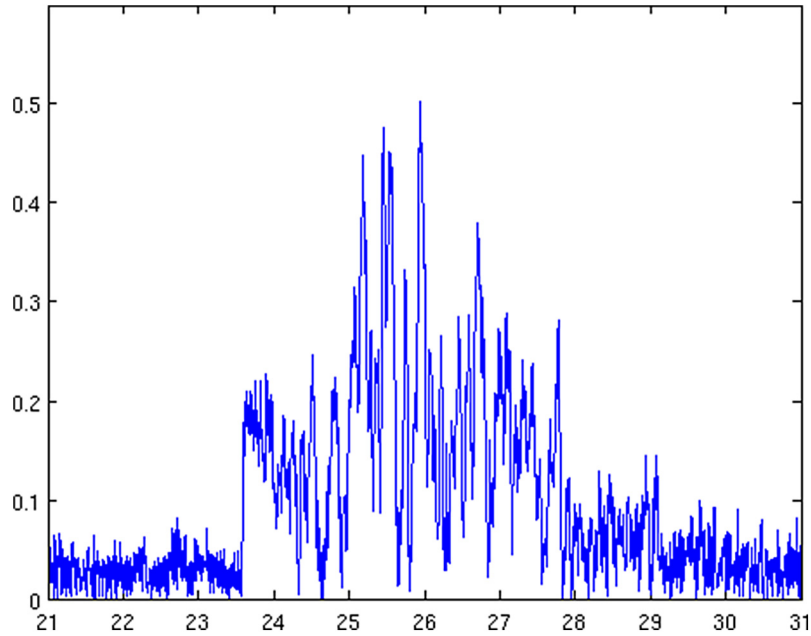

Figure 3.7. A typical overdense meteor echo. The vertical axis is power in arbitrary units while the horizontal axis is time in seconds.

Belgian territory. Figure 3.8 shows the position of the transmitter and of the 26 receiving stations in August 2018.

The transmitter is a crossed-dipole antenna with an 8 m × 8 m metallic grid acting as the reflector. It emits a pure sinusoidal wave with no modulation at a frequency of 49.97 MHz and with a power of approximately 150 W. The choice of the frequency was based on several physical and practical reasons. First, the frequency is high enough to avoid any reflection on the ionospheric layers (the E region peak is approximately at the same height as the meteor zone). Second, as can be seen from equation (3.1), the power of an underdense meteor echo scales as λ^3 and its duration (measured by the time constant of the exponential decay) scales as λ^2. Consequently, for a given meteor and trajectory, if the frequency was 150 MHz instead of ~50 MHz, the received signal would be 27 times less powerful and its duration 9 times shorter. Finally, the frequency must be available and protected.

The decision to use an 8 m × 8 m metallic grid for the reflector was prompted by the desire to emit the maximum amount of power toward the zenith, to have a relatively broad lobe to cover a large portion of the sky and to not emit too much power horizontally. The simulated vertical and horizontal patterns of the transmitter are shown in figure 3.9. Details of the electromagnetic simulations can be found in [4].

Each receiving station uses the same technology, which is depicted in figure 3.10.

The antenna is a three-element Yagi antenna set up vertically and tilted in azimuth to the direction of the transmitter. It has a broad lobe as well in order to cover a large portion of the sky and capture as many meteor echoes as possible.

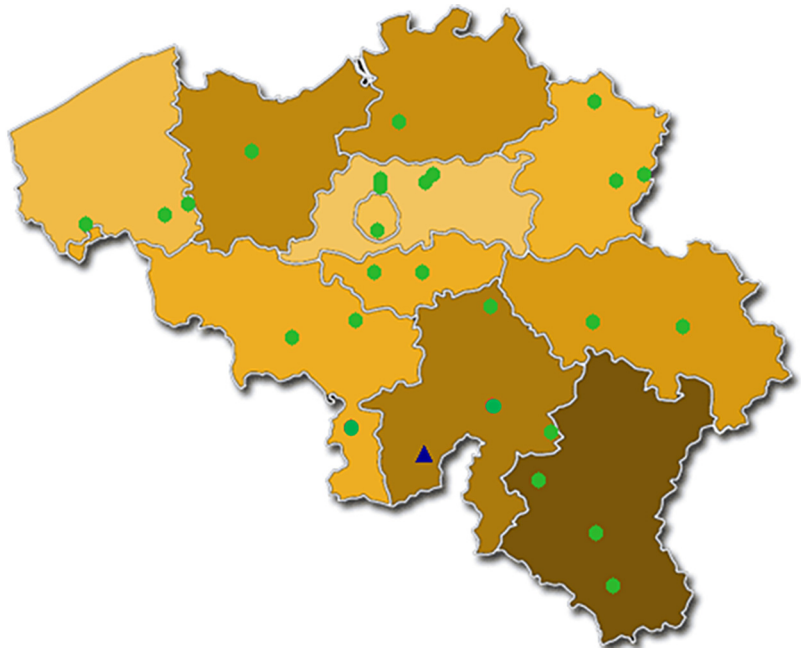

Figure 3.8. Map of the BRAMS network on 30 August 2018. The transmitter is the blue triangle while the green dots are the 26 identical receiving stations.

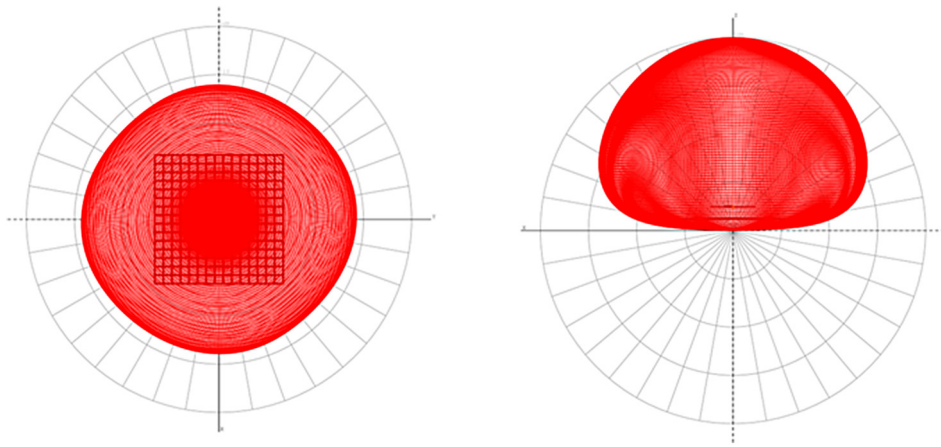

Figure 3.9. Simulations of the horizontal (left) and vertical (right) patterns of the BRAMS transmitter [4].

It has nulls along the direction of the elements of the antenna and the reflector protects from unwanted reflections on the ground. The simulated horizontal and vertical patterns of the antenna are shown in figure 3.11.

The antenna is connected to a commercial ICOM-R75 receiver whose local oscillator frequency is set to 49.969 MHz in order to shift the frequencies from

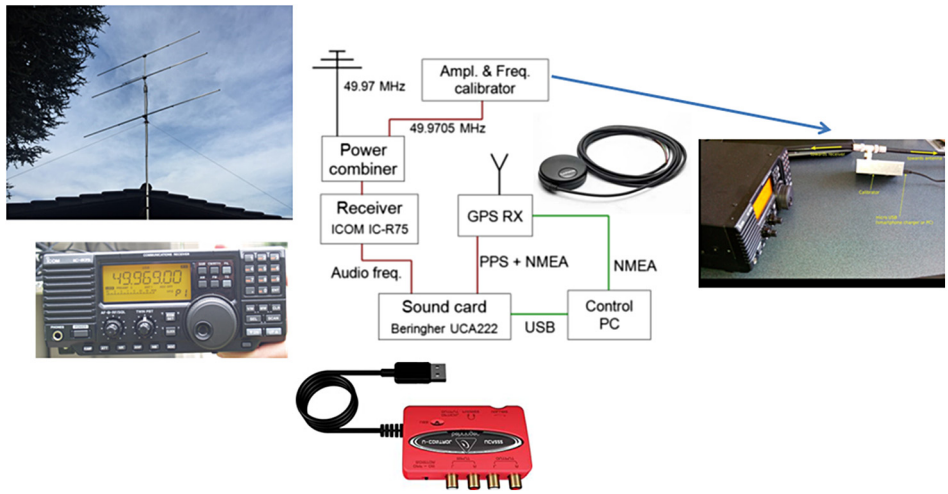

Figure 3.10. Technology used by each BRAMS receiving station.

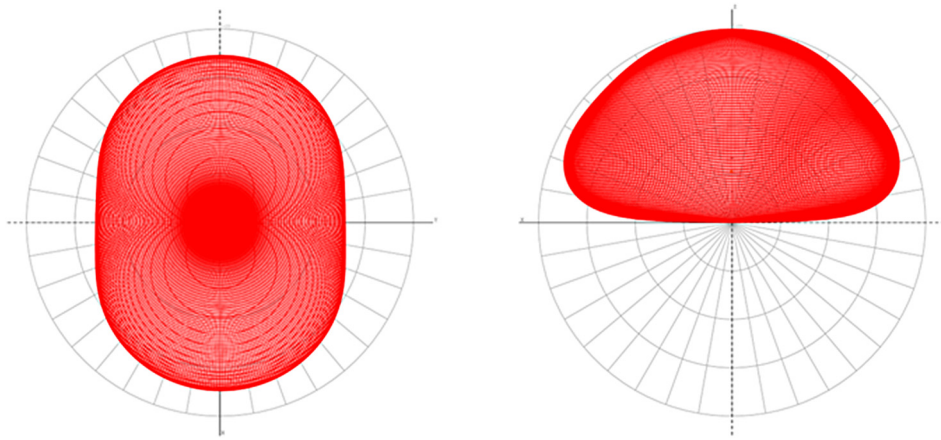

Figure 3.11. Simulations of the horizontal (left) and vertical (right) patterns of the BRAMS receiving antennas [4].

around 49.97 MHz to around 1 KHz using a frequency mixer. The advantage of shifting down the signal to lower frequencies is that it can then be sampled using a cheap external Behringer UCA222 soundcard. The sampling frequency is 5512 Hz. Each BRAMS station is also equipped with a GPS clock which provides a very accurate pulse per second (PPS) signal, allowing all the BRAMS stations to be synchronized. The signals coming from the receiver and from the GPS clock are sampled simultaneously using the two stereo input entries of the soundcard. The soundcard is controlled by free software called Spectrum Lab (SL) running on Windows on a local PC. An additional device called the BRAMS calibrator is added to the signal coming from the antenna via a Tee. This device is designed in order to

produce a signal at a unique frequency which is very stable both in frequency and amplitude. By construction this signal is emitted approximately 500 Hz above the signal of our transmitter, hence at 49.9705 MHz. It provides an accurate reference for frequency measurements (useful, for example, to measure a Doppler effect) and a continuous measurement of the gain of the receiving chain (receiver + soundcard).

3.2.2 The BRAMS data

BRAMS data are saved locally on a PC by SL under an audio WAV format. Data are saved every 5 min which means that 288 WAV files are saved every day at each station. An example of BRAMS data is shown in figure 3.12. Amplitude is plotted in arbitrary units as function of the sample number. Since each file lasts approximately 300 s, the total number of samples in a WAV file is of the order of $300 \times 5512 \sim 1.6$ million. Note that this is the amplitude that is recorded (as a voltage measurement in the receiver) which therefore can take positive and negative values. We are interested in the power profile of the meteor echoes, which is simply the square of these data.

Figure 3.12 clearly indicates that the recorded signal is very noisy and it is hard to distinguish meteor echoes from other spurious signals. A much better representation is to generate a spectrogram from the raw BRAMS data. For that, a fast Fourier transform (FFT) is carried out on 16 384 (2^{14}) samples and by stacking consecutive FFT, the spectrogram can be obtained and displays how the power of the signal is distributed among frequencies as a function of time. The power is color-coded. The

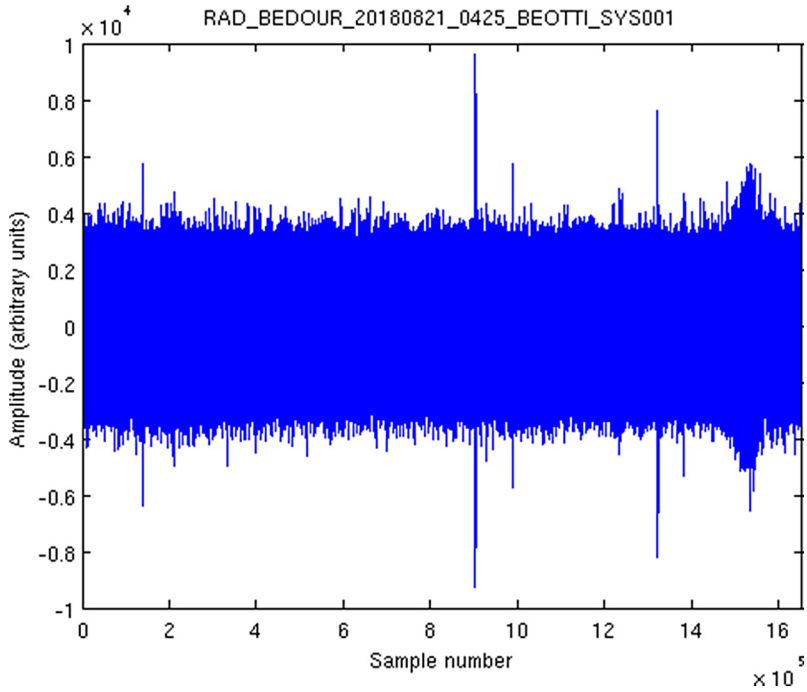

Figure 3.12. Example of raw BRAMS data. Station: BEOTTI. Date: 21/08/2018 at 04:25 UT.

time resolution Δt of the spectrogram is much worse than in the raw data and is equal to 16 384/5512 ~ 2.97 s. Conversely, the frequency resolution Δf is quite good and equal to 5512/16 384 ~ 0.34 Hz. In BRAMS data, however, an overlap of 90% is added in order to smooth the signals in the spectrogram. This means that each FFT includes only 10% of new points and 90% of common points with the previous FFT. By doing this, the apparent time resolution $\Delta f'$ becomes equal to ~0.3 s. In practice the power is simply spread over consecutive columns of the spectrogram so a meteor echo will appear on several consecutive columns of the spectrogram. In figure 3.13, the spectrogram corresponding to the raw data from figure 3.12 is displayed. The spectrogram is constructed to show a 200 Hz range centered on the horizontal signal, which is the direct (tropospheric) signal coming from the transmitter. In this example it appears at around 1262 Hz and not 1 KHz as previously explained. The reason is that the local oscillator (LO) of the ICOM-R75 receiver is not perfectly stable and is strongly influenced by the temperature of the receiver. As a consequence, the LO drifts and appears at a larger frequency. These LO drifts can be easily monitored by measuring the frequency of the calibrator signal. The long lasting signals in figure 3.13, although sometimes discontinuous, are reflections on airplanes flying near the transmitter. Since the distances between the transmitter and all BRAMS stations are lower than 250 km, airplanes flying at an altitude of around 10 km will never appear below the horizon. These reflections are spurious signals which strongly complicate the analysis of BRAMS data. The nearly vertical signals are all underdense meteor

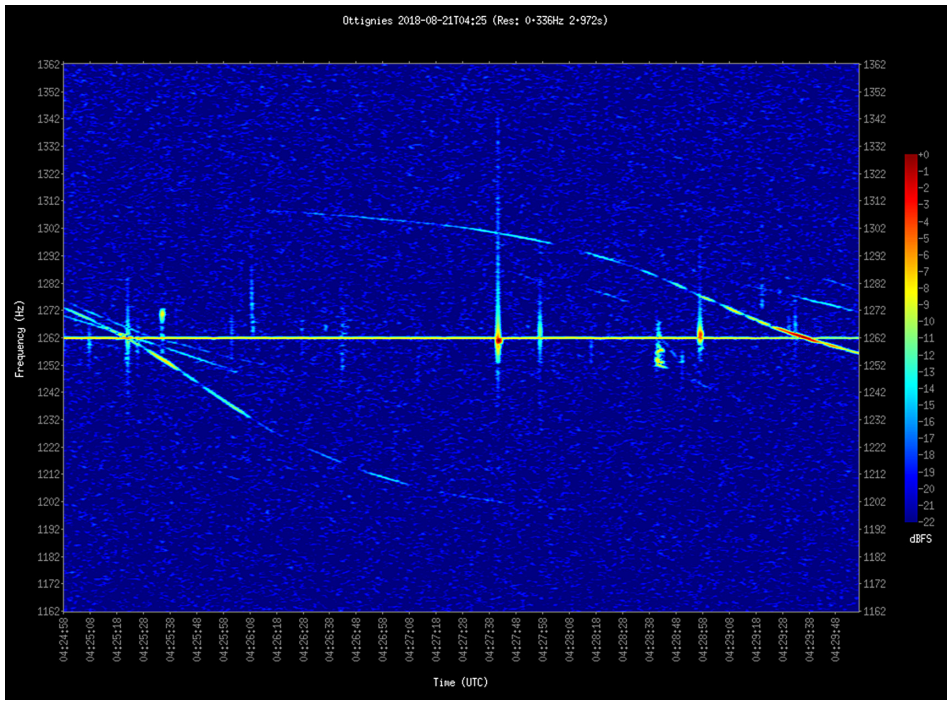

Figure 3.13. Example of BRAMS spectrogram. Station: BEOTTI. Date: 21/08/2018 at 04:25 UT.

echoes while the one with a more complex shape on the right-hand side of the spectrogram is an overdense meteor echo.

Figure 3.13 displays only the 200 Hz range because that range is sufficient to encompass all of the trail meteor echoes. Indeed, the vertical position of a meteor echo in a spectrogram depends on the Doppler effect due to the speed of the meteor trail, hence on the speed v_w of mesospheric/thermospheric winds. If we take a typical value of 100 m s^{-1} for v_w, the maximum Doppler associated effect is $\Delta f = 2 \times f \times v_{wr}/c$, where $f = 49.97$ MHz, v_{wr} is the radial component of the wind speed and c is the speed of light. The factor 2 is a rough estimate and comes from the fact that there is a double Doppler effect, first between the transmitter and the moving trail, then between the moving trail and the receiver. This provides a value of ~33 Hz. So, trail meteor echoes will never appear outside a range of ±100 Hz from the direct signal. The situation is different for head echoes for which the associated speeds and Doppler effects are much larger. Nevertheless these are rarely detected with BRAMS and will not be discussed here.

With a sampling frequency $f_s = 5512$ Hz, Nyquist's theorem tells us that we have in theory access to all frequencies between 0 and $f_s/2 = 2756$ Hz. Figure 3.14 displays the same spectrogram as figure 3.13 but showing a larger frequency span going from 900 to 1800 Hz. The signal just below 1750 Hz is the signal from the BRAMS calibrator.

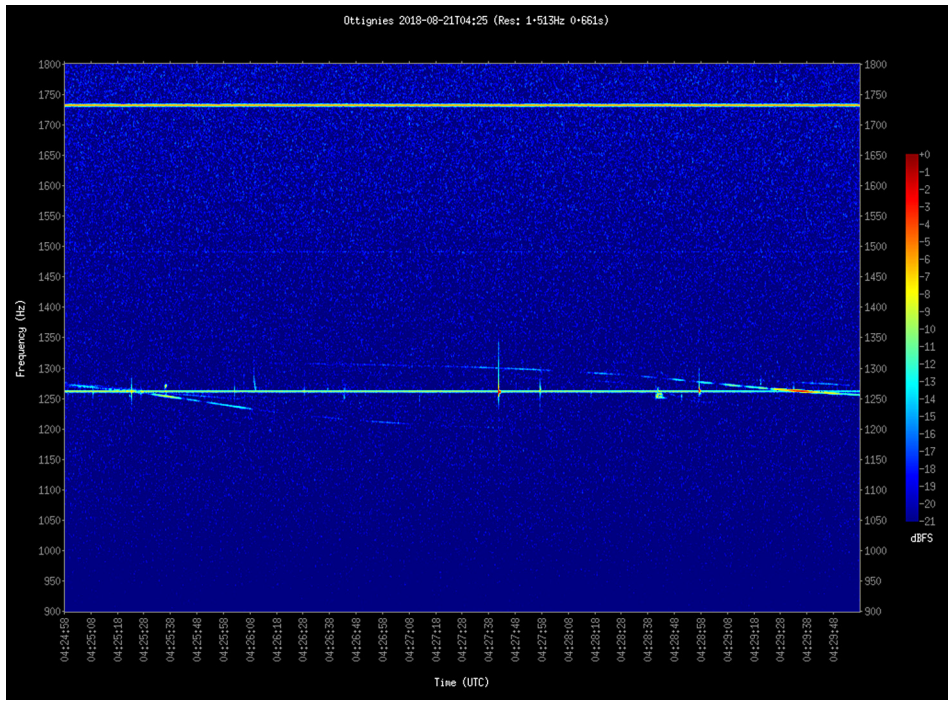

Figure 3.14. The same spectrogram as in figure 3.13 but with a larger frequency range. The signal near 1740 Hz is the BRAMS calibrator.

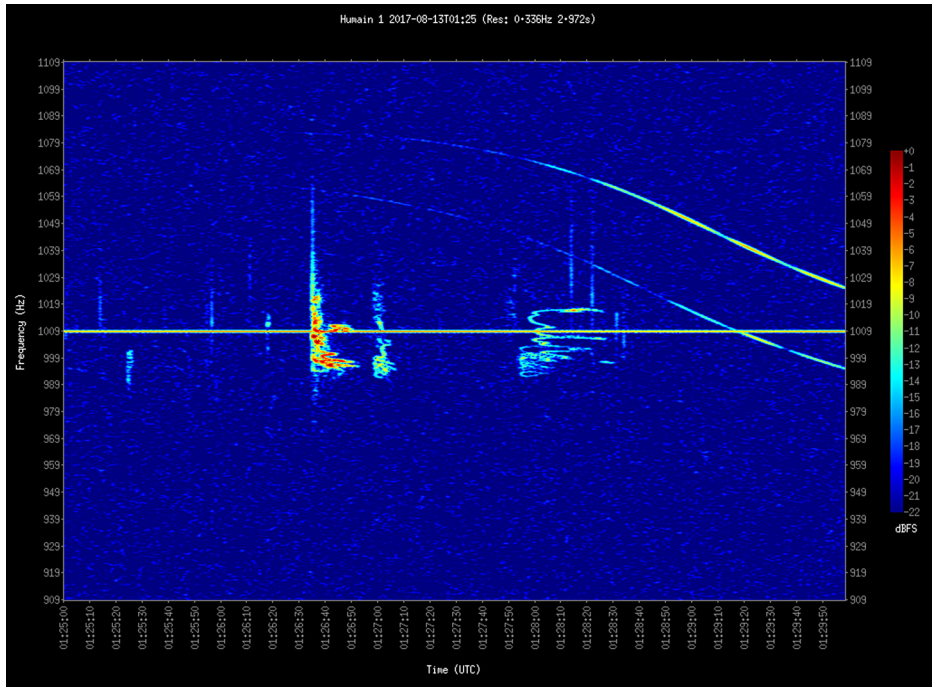

Figure 3.15. Example of BRAMS spectrogram during the Perseids 2017. Station: BEHUMA. Date: 13/08/2017 at 01:25 UT.

During meteor showers, the number of overdense meteor echoes strongly increases, as can be seen for example in figure 3.15, obtained during the Perseids 2017.

3.2.3 Determination of meteoroid trajectories using BRAMS data

One of the main objectives of the BRAMS project is to reconstruct meteoroid trajectories. Due to the specular reflection, a single receiving station is only sensitive to one point of the trajectory. However, since the position of each specular reflection point depends on the geometry and will therefore vary along the meteoroid path for each station, it is in principle possible to reconstruct the trajectory from observations of the same meteor at various stations. To reconstruct the trajectory at least six stations need to detect the same meteor in order to obtain the coordinate of one point (three unknowns), one direction (two angles) and the speed (assuming the deceleration is negligible, otherwise additional parameters should be included). This is a reason why the BRAMS network has to be relatively dense in order to maximize the chances of obtaining at least six multiple detections.

In [5], an attempt is made to use a suggestion proposed by Nedeljkovic [6]. The idea is the following: when the meteoroid trajectory L is known, finding the position of the specular point for a given transmitter (T) and receiver (R) pair requires only to find the point on the trajectory that is tangent to the ellipsoid with T and R as foci (see figure 3.1). It is called the direct problem and has a simple analytical solution.

The inverse problem of retrieving a trajectory that is tangential to a set of ellipsoids with foci T and R_1, R_2, … is much more complex (R_i being the position of receiver i). Instead, a set of possible trajectories is generated and only the ones tangential to a number of ellipsoids corresponding to the number of receiving stations with detections are selected. The selection criterion is that the altitude of the specular reflection point must be within the meteor zone, otherwise the corresponding trajectories are rejected. The higher the number of stations considered, the lower the number of remaining trajectories. The advantage of this method is that it uses only the direct problem. The disadvantage is that a very large number of trajectories have to be generated first. Among all possible remaining trajectories, an assumption on the speed of the meteoroid can be made to generate time delays between two receiving stations. Indeed, for two stations R_1 and R_2, the specular reflection points are located at different positions on the meteoroid trajectory. Therefore, the meteor echo will appear first at station R_1 then at station R_2 when the meteoroid has traveled the distance between the two reflection points. This additional condition of the time delays allow one to reduce the number of remaining possible trajectories. This work is still on-going.

One station, located in the radio-astronomical site of Humain, in the south-east of Belgium, is a radio interferometer which, unlike all other BRAMS stations, is able to retrieve the direction of arrival of a meteor echo to an accuracy of the order of 1°. It is made of five Yagi antennas, three of them aligned along two orthogonal axes, roughly aligned N–S and E–W, with the central antenna common to the two axes. The principle of the interferometer is based on measuring phase differences between two pairs of antennas from the three co-aligned antennas. Then, using the method proposed by Jones *et al* [7], it is possible to determine accurately and unambiguously the projections of the angle of arrival of the meteor echo in the N–S and E–W planes (see [8] for more details about the technique and the interferometer itself). The principle is illustrated in figure 3.16 with three antennas named '0', '1' and '2'. The projection of the angle of arrival in the plane of the three antennas is called ξ.

From the projections ξ_1 and ξ_2 in the two orthogonal planes, the azimuth α and elevation β of the angle of arrival of the meteor echo can be determined using (e.g. [9])

$$\alpha = \cos^{-1}\left(\frac{\cos\xi_1}{\cos\beta}\right) = \cos^{-1}\left(\frac{\cos\xi_2}{\cos\beta}\right) \tag{3.5}$$

$$\beta = \tan^{-1}\left(\frac{\cos\xi_2}{\cos\xi_1}\right). \tag{3.6}$$

An example of results is shown below for an underdense meteor echo obtained on 5 December 2016, corresponding to the second white rectangle counted from the left in the spectrogram shown in figure 3.17. It corresponds to a bright meteor echo that does not overlap in frequency with any other signal, such as a reflection on an airplane or the direct signal coming from the transmitter.

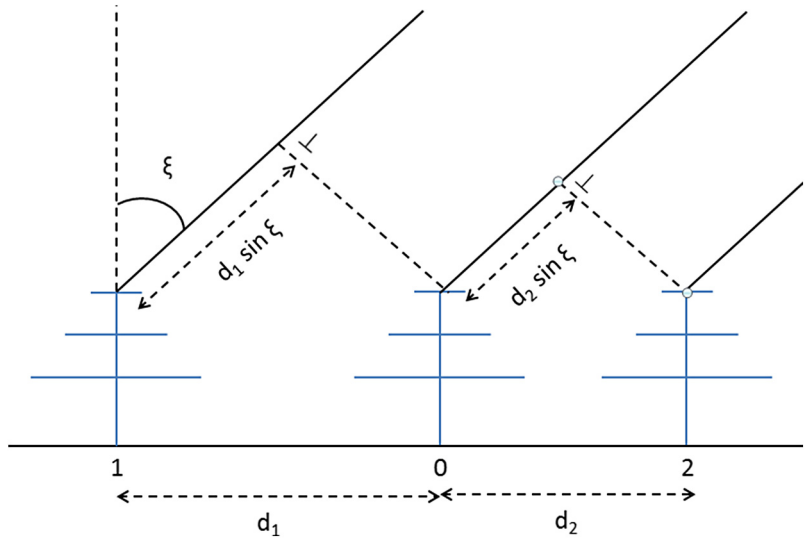

Figure 3.16. Sketch of a linear array of three antennas with the central antenna 0 being the phase reference. This principle is used along two orthogonal axes for the radio interferometer in Humain (with antenna '0' being common to the two axes).

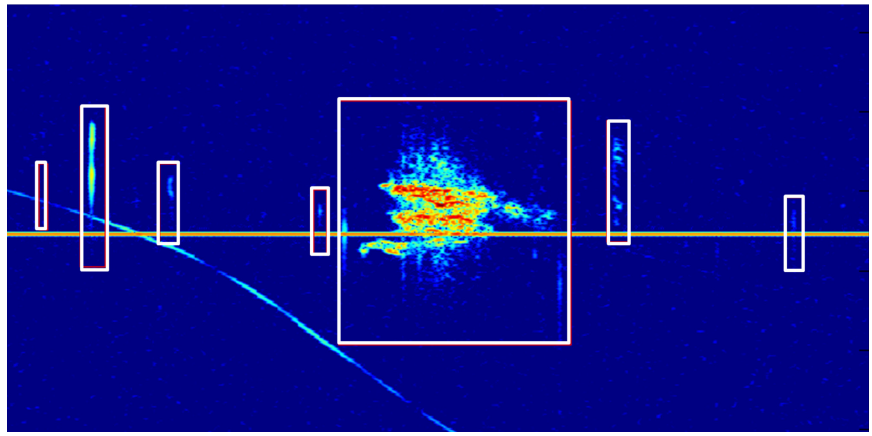

Figure 3.17. Spectrogram obtained at Humain on December 5, 2016, 00h35 UT. Rectangles are aggregated results from individual contributions from a Citizen Science project called the Radio Meteor Zoo (http://www.radiometeorzoo.eu).

Spectrograms are useful here in order to determine the best frequency to use to calculate the phase. Since the phase of the meteor echo should not depend on frequency, the best procedure would consist in selecting the frequency bin in which the signal-to-noise ratio (S/N) is the highest. The results for the phase differences between antenna pairs are shown in figure 3.18.

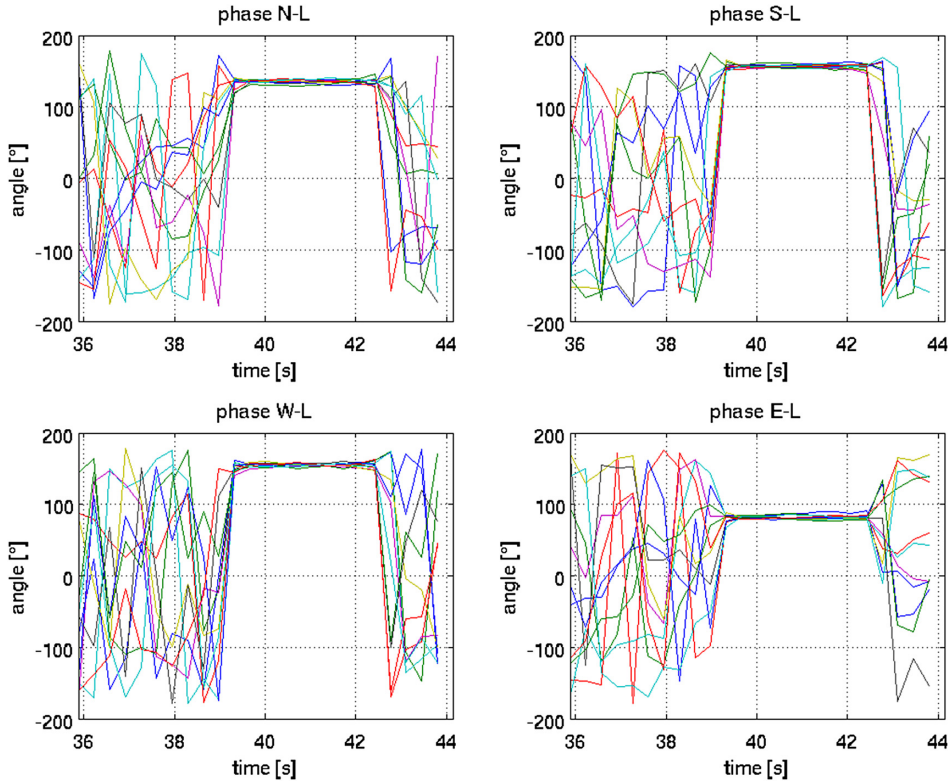

Figure 3.18. Phase differences between the central antenna L and (top left) the north (N) antenna; (top right) the south (S) antenna; (bottom left) the east antenna; and (bottom right) the west antenna, for data from figure 3.16. The ten different curves correspond to adjacent frequency bins centered on the upper bright spot of the meteor echo shown in the second rectangle of figure 3.16.

For the selected frequencies, just before and after the meteor echo, only noise is recorded and, therefore, the phase differences vary completely randomly as expected. During the meteor echo, however, the phase differences become strongly coherent. The Jones method is applied to these results to obtain the two angles of arrival ξ_{N-S} and ξ_{E-W} in the two perpendicular planes, which are then combined to provide the elevation angle and the azimuth angle of the meteor echo using equations (3.5) and (3.6). The results are shown in figure 3.19 for the frequency with the highest S/N (called FreqOfi). The results at other adjacent frequencies are very similar. Again, the results are very stable during the meteor echo which gives confidence in the method.

The example presented here consists of an 'isolated' meteor echo which does not overlap with any other spurious signal. In practice, an overlap occurs quite often with, e.g., an airplane reflection or with the direct signal from the beacon. For these meteor echoes, an automated procedure is currently being developed in order to select the frequency bin with the highest S/N and that belongs to the meteor echo.

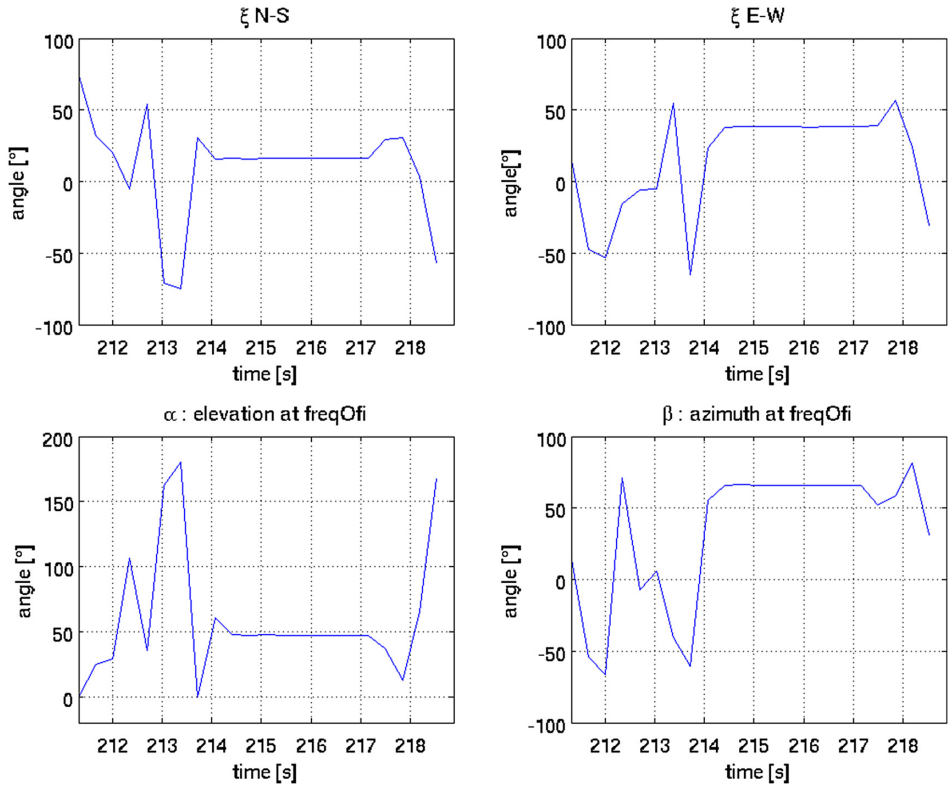

Figure 3.19. Top: Angles of arrival, ξ_{N-S} and ξ_{E-W}, as a function of time for data from figure 3.16. Bottom: Corresponding elevation (α) and azimuth (β) angles.

The directions of arrival computed for the meteor echoes with the BRAMS interferometer are thus far not calibrated. There are a number of systematic errors that need to be taken into account and corrected for. This includes a small difference in length between the cables going from antennas to receivers, an imperfect alignment of the antennas (in X, Y and Z), and an imperfect alignment of the axes with the N–S and E–W directions. A precise determination of these systematic errors was carried out in 2018, but has not yet been implemented in the results presented here. The algorithms are currently modified to correct for these systematic errors. Once they are taken on board, the calibration itself can be performed with one of the following methods: (1) using the BRAMS calibrator [10] as a transmitter and a calibrated antenna both attached to a drone flying in the far-field of the interferometer; (2) using the signal reflected from a plane whose position can be accurately determined (e.g. using websites such as Flight Tracker); or (3) using data from optical cameras located next to the interferometer. The first two methods are currently under investigation. The third one was used, e.g., by Madkour *et al* [9].

The results from the radio interferometer in Humain will be extremely important for the retrieval of individual meteoroid trajectories as only data from three additional traditional BRAMS receiving stations are then needed [11].

3.2.4 Comparisons of optical observations with BRAMS data

When the algorithms to retrieve meteoroid trajectories are operational, they need to be carefully checked. One possibility is to compare trajectories retrieved with BRAMS observations to those obtained with optical networks. For that purpose, BRAMS has partnered with the CAMS-BeNeLux network. CAMS (Cameras for Allsky Meteor Surveillance) is a network of optical video cameras that is able to measure the meteoroid trajectory very accurately, speed and deceleration in the Earth's atmosphere. With these measurements, accurate orbits can be computed with the end goals of validating unconfirmed meteor showers, detecting new ones and identifying their parent bodies [12, 13]. CAMS was initially developed in the US and funded by NASA, but an equivalent network has been developed in the BeNeLux since March 2012, mostly funded by motivated amateurs [14]. CAMS-BeNeLux detects a lot of meteoroid trajectories passing above or near Belgium and therefore potentially detectable by the BRAMS network. An example of such common detections is shown in figure 3.20.

In addition, another study can be done combining CAMS-BeNeLux and BRAMS observations. Indeed, with the trajectories provided by CAMS-BeNeLux, the calculations of the theoretical specular reflection points for all

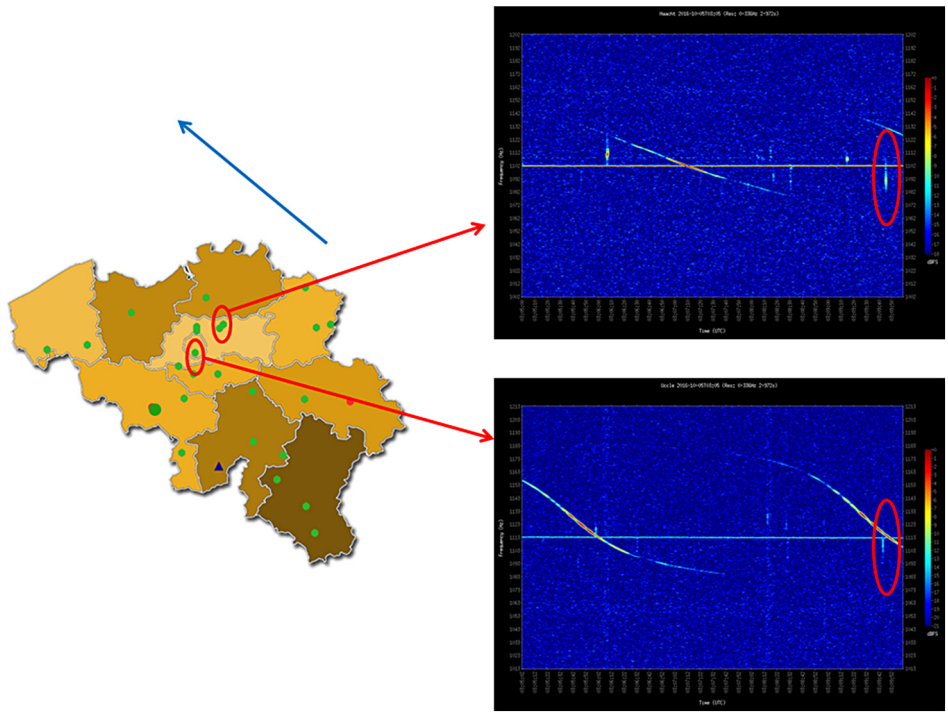

Figure 3.20. Comparison between BRAMS and CAMS observations. The blue line is the projection on the ground of a visual CAMS trajectory obtained on 5 October 2016. On the right two spectrograms from BRAMS stations BEHAAC and BEUCCL are shown. The meteor echoes are clearly visible. Note the different Doppler effect due to the geometry.

BRAMS stations are straightforward using the forward model described previously. With the speed and deceleration measurements, the time delays expected between the appearances of the meteor echoes at all BRAMS stations can also be computed. From the power profiles of the corresponding meteor echoes, the peak values can be measured. For underdense meteor echoes, equation (3.1) can be used, since in this case the whole geometry is known (so R_T, R_R, ϕ and β can be computed). Using simulated antenna gains for G_T and G_R in the direction to the specular reflection point, and making a reasonable assumption on the polarization of the radio wave, an estimate of the line electron density α can be obtained. This can be done for every BRAMS receiving station which detects the meteor, hence several measurements of α at different locations (specular reflection points) on the meteoroid path can be obtained. This set of values can then be compared to an ablation model using the same parameters for the trajectory and entry speed of the meteoroid and assuming a typical composition. By adjusting the mass as the last free parameter, a fit of the model results to the set of electron line density values can be carried out to obtain an estimate of the initial mass of the object.

Another optical network of interest is FRIPON (Fireball Recovery and InterPlanetary Observation Network, https://www.fripon.org/, see e.g. [15]). FRIPON is a dense French network with one hundred all-sky optical cameras set all over France with an average distance of ~100 km. The main objective is to

Figure 3.21. Example of a fireball detection with the FRIPON camera in Brussels on 20 October 2017 at 00H38 UT (Credit: François Colas).

determine trajectories of fireballs and try to recover on the ground potential associated meteoroids. Recently, FRIPON has been extended to various European countries including Italy, Spain, Austria, the Netherlands, Germany and Belgium. One of the FRIPON cameras was set up in Brussels in 2016. Again a comparison between FRIPON optical observations and BRAMS radio observations is planned. Note that in the case of fireballs, the associated radio meteor echoes are always overdense and a head echo is very often observed before the trail echo. An example of a fireball on 20 October 2017 by the FRIPON camera in Brussels is shown in figure 3.21.

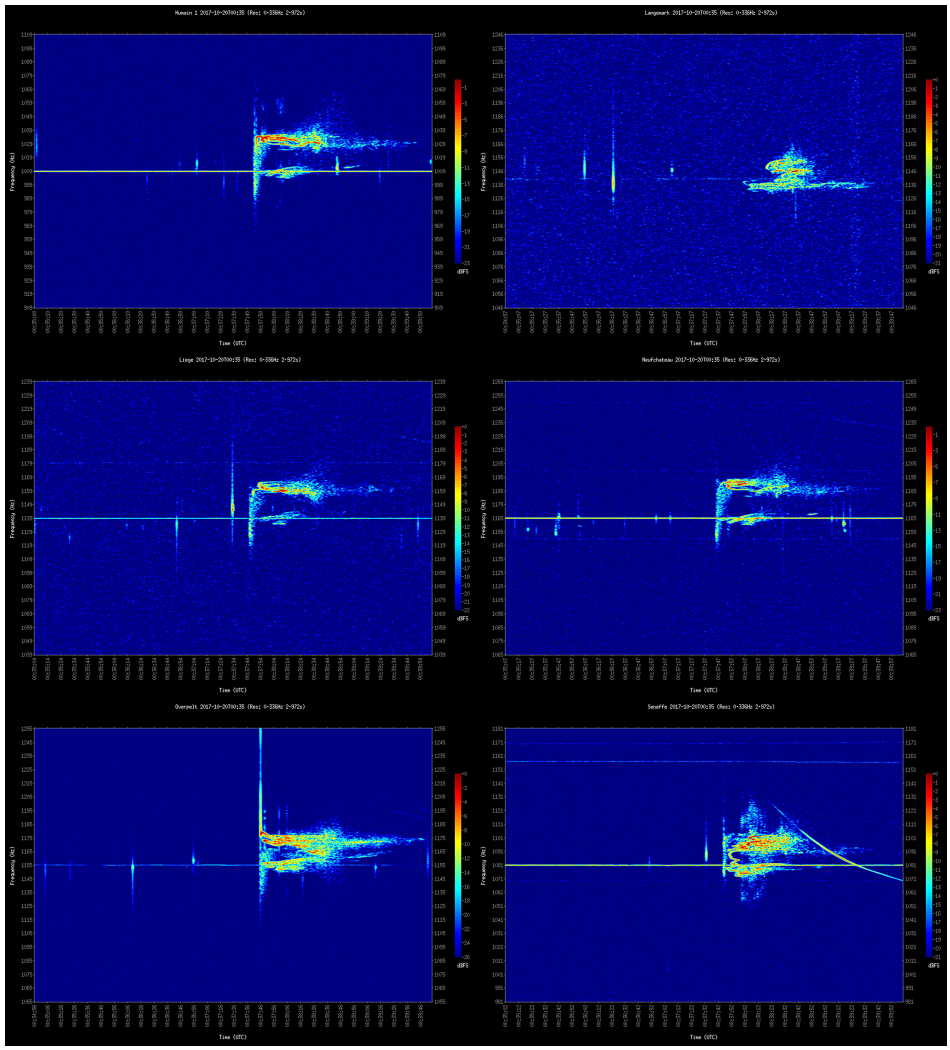

Figure 3.22. Spectrograms obtained with the BRAMS network on 20 October 2017 at 00H35 UT. The overdense meteor echoes associated with the fireball at ~00H38 are clearly visible. Stations: (left, from top to bottom) Humain, Liège and Overpelt; (right, from top to bottom) Langemark, Neufchâteau and Seneffe.

Six examples of corresponding radio observations with the BRAMS network are shown in figure 3.22. Note the variety of the complex shapes of the meteor echoes at different stations due to the different geometries. A head echo is also clearly visible in the data from the Overpelt station (bottom left spectrogram).

3.3 Conclusions

Radio observations of meteor echoes have the double advantage over optical observations that they can be carried out continuously and that they are sensitive to smaller objects that produce enough ionization but not enough light. BRAMS is a fairly recent network using forward scatter radio observations and provides a lot of useful data, mostly about meteor trail echoes. In the future, comparison of radio data with optical data provided by either the CAMS-BeNeLux or the FRIPON network, or with results from complex modeling of the meteoroid ablation, will undoubtedly produce very important new results.

Acknowledgements

BRAMS is a project of the Royal Belgian Institute for Space Aeronomy (BIRA-IASB) and has been funded mostly by the Solar-Terrestrial Center of Excellence (STCE).

The author would like to thank the organizers of the 61st Course of the International School of Quantum Electronics on *Hypersonic Meteoroid Entry Physics* for their kind invitation and giving him the opportunity to visit such a wonderful place as the Ettore Majorana Centre in beautiful Erice.

The author is indebted to all the people at BIRA-IASB who have actively contributed to the development of the BRAMS project and therefore to this publication: Sylvain Ranvier, Michel Anciaux, Emmanuel Gamby, Stijn Calders, Cédric Tétard, Antoine Calegaro and Johan De Keyser. The author would also like to thank Antonio Martinez Picar and Cis Verbeeck from the Royal Observatory of Belgium for their constant support and suggestions in developing the tools to analyze the BRAMS data. Finally, the author would like to thank the CAMS-BeNeLux team and the FRIPON team at IMCCE (Institut de Mécanique Céleste et de Calcul des Éphémérides) for their active collaboration.

References

[1] McKinley D W R 1961 *Meteor Science and Engineering* (New York: McGraw-Hill)

[2] Pecina P 2015 An analytical theory of radio-wave scattering from meteoric ionization–I. Basic equation *Mon. Not. R. Astron. Soc.* **455** 2200–6

[3] Webster A R, Brown P G, Jones J, Ellis K J and Campbell-Brown M 2004 Canadian meteor orbit radar (CMOR) *Atmos. Chem. Phys.* **4** 679–84

[4] Martínez Picar A, Ranvier S, Anciaux M and Lamy H 2014 Modeling and calibration of BRAMS antenna systems, *Proc. of the Int. Meteor Conf., (Giron, France)* Rault J-L and Roggemans P pp 201–6

[5] Lamy H and Tétard C 2016 Retrieving meteoroids trajectories using BRAMS data: preliminary simulations, *Int. Meteor Conf.*, *(Egmond, the Netherlands)* Roggemans A and Roggemans P pp 149–52
[6] Nedeljkovic S 2006 Meteor forward scattering at multiple frequencies, *Proc. of the Int. Meteor Conf., 24th IMC*, *(Oostmalle, Belgium)* Verbeeck C and Wislez J-M pp 108–16
[7] Jones J, Webster A R and Hocking W K 1998 An improved interferometer design for use with meteor radars *Radio Sci.* **33** 55–65
[8] Lamy H, Tétard C, Anciaux M, Ranvier S, Martinez Picar A, Calders S and Verbeeck C 2018 First observations with the BRAMS radio interferometer, *Proc. of the Int. Meteor Conf.*, *(Petnica, Serbia)*
[9] Madkour W, Yamamoto M-y, Kakinami Y and Mizumoto S 2016 A low cost meteor observation system using radio forward scattering and the interferometry technique *Exp. Astron.* **41** 243–57
[10] Lamy H, Anciaux M, Ranvier S, Calders S, Gamby E, Martinez Picar A and Verbeeck C 2015 Recent advances in the BRAMS network, *Int. Meteor Conf.*, *(Mistelbach, Austria)* Rault J-L and Roggemans P pp 171–5
[11] Wislez J-M 2006 Meteor astronomy using a forward scatter set-up, *Proc. of the Radio Meteor School*, *(Oostmalle)* Verbeeck C and Wislez J-M pp 84–106
[12] Jenniskens P, Gural P S, Dynneson L, Grigsby B J, Newman K E, Borden M, Koop M and Holman D 2011 CAMS: Cameras for Allsky Meteor Surveillance to establish minor meteor showers *Icarus* **216** 40–61
[13] Jenniskens P, Nénon Q, Albers J, Gural P S, Haberman B, Holman D, Morales R, Grigsby B J, Samuels D and Johannink C 2016 The established meteor showers as observed by CAMS *Icarus* **266** 331–54
[14] Roggemans P, Johannink C and Breukers M 2016 Status of the CAMS-BeNeLux network, *Int. Meteor Conf.*, *(Egmond, the Netherlands)* Rault J-L and Roggemans P pp 254–60
[15] Colas F *et al* 2015 French fireball network FRIPON, *Int. Meteor Conf.*, *(Mistelbach, Austria)* Rault J-L and Roggemans P pp 37–40